Etching of Transition Metal Dichalcogenide Monolayers into Nanoribbon Arrays

SCHOLARONE™
Manuscripts

Conceptual Insights

Transition metal dichalcogenide (TMDC) nanoribbons has been widely studied by computational scientists for their novel physical and electronic characters distinct from the bulk. Existing synthesis methods for TMDC nanoribbons either require a growth template, which sometimes is undesirable for electronic applications, or ion-beam etching with low efficiency and edge controllability. Different from the reported bottom-up and top-down methods, we turn to liquid phase etching method for the production of TMDC nanoribbons. This method uses a low-cost reducing agent solution and tears the TMDC monolayers on a Si wafer within minutes through a mechano-chemical process. This method overcomes the limitation of sample size and time of ion-beam etching, while retains the high crystal quality of CVD grown TMDC on Si wafer and gives a consistent zigzag edge. Through different reducing agents and solvents, this work explores the chemistry of reducing agents with TMDC, helping researchers understand the decomposition mechanism of ultra-thin nanomaterials and providing them a new pathway in manipulating the geometry of 2D nanomaterials.

Nanoscale Horizons

Etching of Transition Metal Dichalcogenide Monolayers into Nanoribbon Arrays

Zixing Wang,[a] Xiang Zhang,[b] Jordan A. Hachtel,[c] Amey Apte,[b] Chandra S. Tiwary,[b] Robert Vajtai,[b] Juan Carlos Idrobo,[c] Ramazan Ozturk,[*, b] and Pulickel Ajayan[*, b]

[a] Department of Chemistry, Rice University, 6100 Main Street, Houston, TX 77005, United States
[b] Department of Materials Science and Nano Engineering, Rice University, Houston, TX 77005, United States
[c] Center for Nanophase Materials Sciences, Oak Ridge National Laboratory, Oak Ridge, TN 37830, United States
+ Electronic Supplementary Information (ESI) available: [details of any supplementary information available should be included here]. See DOI: 10.1039/x0xx00000x

Two-dimensional transition metal dichalcogenide (TMDC) nanoribbons are reported to exhibit interesting properties distinctly different from their 2D analogues, including a change of transport properties depending on the edge structure, enhanced exciton correlation effect and thermoelectric property. Here we report a successful preparation method for large arrays of 2D TMDC nanoribbons without template, using a reducing agent aqueous etchant. This method is a simple and tuneable way for generating TMDC (e.g. MoS_2 and $MoSe_2$) nanoribbons from CVD grown 2D TMDCs on Si/SiO_2 through liquid phase mechano-chemical reaction. The reducing agent converts Mo(IV) from the defect sites to a lower oxidation state, thus expanding the defects. Water acts as a detaching and tearing medium that pulls the TMDC flake into nanoribbons. The area of conversion, density, and thickness of the nanoribbons can be tuned by concentration and potency of the etchant. The 2D nanoribbons possess high structural integrity, zigzag edges with chalcogen termination, and an increase of bandgap when ribbon width decreases. This method allows a scalable approach for 2D nanoribbons to be prepared for various applications.

Two-dimensional materials have attracted vast attention in research in the past few years for their unusual properties.[1-4] Monolayer TMDCs composed of molybdenum and tungsten have gained particular interest due to their highly tunable direct band gap that can range 1.1 eV to 1.9 eV,[5] which makes them ideal candidates for transistors, photodetectors, and electron luminescent devices.[5-8] These versatile applications have made routes to synthesize 2D materials with controllable physical properties, such as mechanical and liquid exfoliation, atomic layer deposition (ALD), and chemical vapor deposition (CVD), well-developed but ever expanding fields.[9-14]

One method to control the properties of 2D materials is to reduce the dimensionality and increase the aspect ratio. One dimensional structures formed from 2D materials are expected to exhibit interesting properties and applications that differ from the parent 2D materials.[15-18] Atomically thin nanoribbons, with a higher edge-to-area ratio, have shown promise for applications in electro-catalytic reactions, gas detection, sensing, and energy storage.[19-23] Additionally, theoretical calculations show TMDC nanoribbons have properties that differ from the bulk phase.[16, 24-25] Unlike their 2D counterparts, nanoribbons have optical and electronic properties that are dependent on the geometry and edge structure of the ribbon (i.e. zigzag nanoribbons are ferromagnetic and metallic, while armchair nanoribbons are nonmagnetic and semiconducting).[24] Methods to prepare nanoribbons mostly fall under two categories: bottom-up (templated growth such as pre-patterned amorphous silicon, carbon nanotubes, or Mo nanowires)[26-29] and top-down (ion beam etching: direct helium ion beam milling).[21] The preparation of templates for the bottom-up process is usually tedious, while top-down methods struggle with scalability, which makes generating 1D TMDC structures with controllable geometry and properties without a template an ongoing challenge for fabrication researchers.

In this paper, we demonstrate a scalable, clean, and facile method to convert monolayer 2D MoS_2 sheets into anisotropic nanoribbon arrays using a low-cost aqueous solution of ascorbic acid. A schematic of the process is shown in **Figure 1** (a). Large (several micron) atomically-thin sheets of MoS_2 are prepared using CVD and are selectively etched using an aqueous solution of reducing agents. By varying the concentration and type of the solvents and reducing agents, the width, density, and edge structure of the nanoribbons can be deliberately controlled. The ribbons are characterized via spectroscopy, electron microscopy, and photoluminescence (PL) to investigate the mechanism of the 2D to 1D conversion and demonstrate the tunability of the structure. Finally, the process is also expanded to other TMDC materials, such as $MoSe_2$.
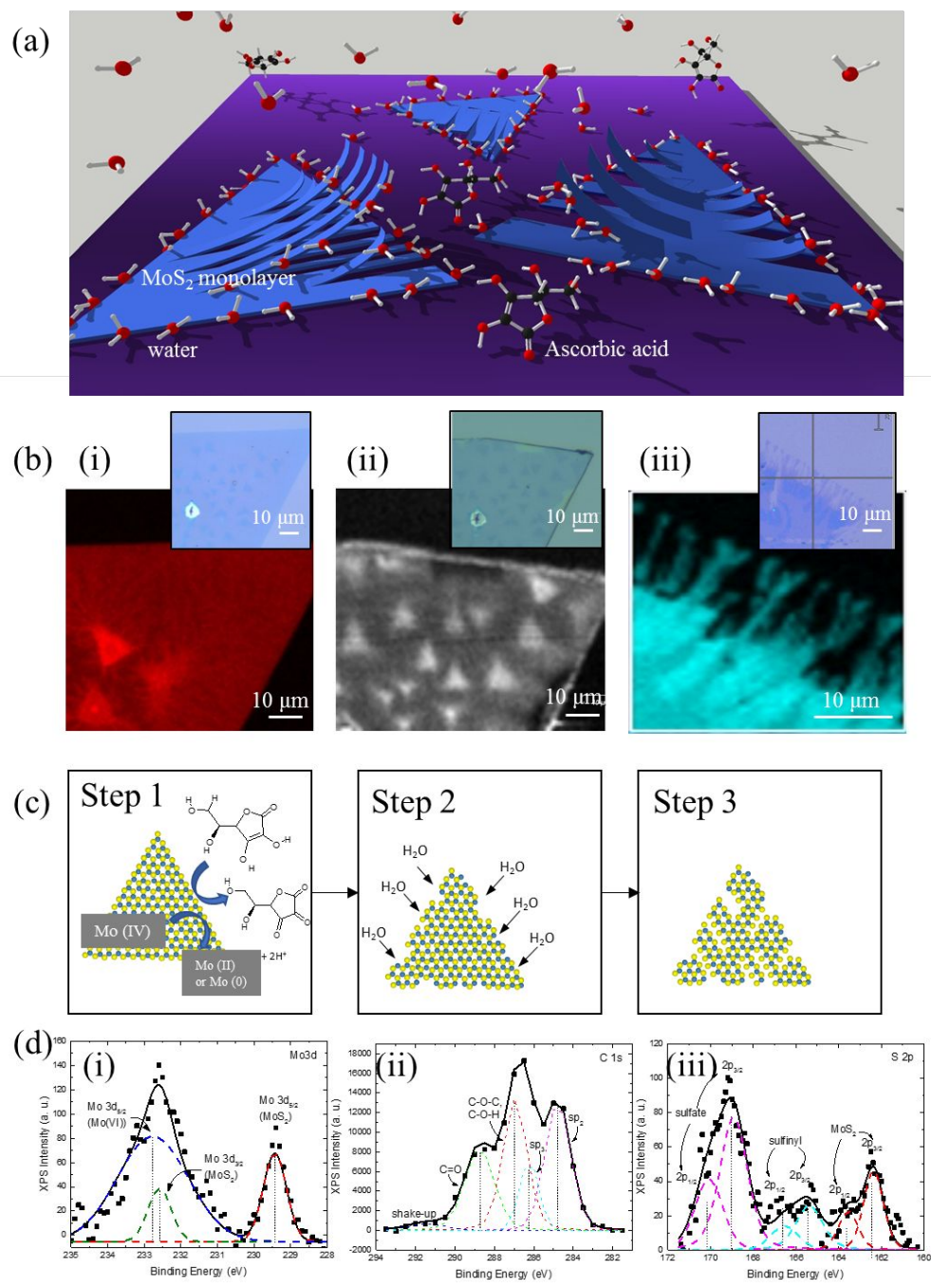
Figure 1. Reaction mechanism of MoS$_2$ nanoribbons. (a) Scheme of the reaction between CVD grown MoS$_2$ and ascorbic acid in

water. (b) Raman mapping at 380 cm^{-1} of MoS$_2$ flakes and their corresponding optical images (top right) (scale bar: 10 µm). (i) MoS$_2$ as grown. (ii) MoS$_2$ treated with 0.5 M ascorbic acid in DMF for 20 minutes. (iii) MoS$_2$ treated with 1.5 mM ascorbic acid in water for 3 minutes. (c) Predicted reaction mechanism of MoS$_2$ monolayers with ascorbic acid aqueous solution. Ascorbic acid first reduces exposed Mo(VI) at the edges of MoS$_2$ flakes and decompose the material. Water then starts tearing the MoS$_2$ ribbons from the defective sites and assists in forming MoS$_2$ nanoribbons. (d) XPS of the end-product of MoS$_2$ powder in 0.05 M ascorbic acid aqueous solution after 12 hours. The Mo spectrum shows 71% Mo transferred from Mo(IV) at 229.43 eV to Mo (VI) at 232.77 eV. The carbon spectrum shows four distinguished peaks at 284.8 eV, 286.2 eV, 287.0 eV and 288.8 eV corresponding to sp$_2$ C-C and C-H, sp$_3$ C-C and C=C, C-O-C and C-O-H, and C=O peaks respectively. Most of S has converted into sulfate due to oxidation after MoS$_2$ degradation. A small amount of sulfinyl was also generated. 21% of the S remained to be in MoS$_2$. This XPS spectrum confirms the reaction between ascorbic acid and MoS$_2$.

CVD grown MoS$_2$ flakes are etched in 1.5 mM ascorbic acid aqueous solution, which is mildly reducing, for three minutes to form nanoribbons (details in **Experimental section**). The effect of solvent and reducing agent was studied respectively to explain the formation mechanism of MoS$_2$ nanoribbons. Water as a strong polar protic solvent detaches CVD grown MoS$_2$ off the SiO$_2$/Si substrate. When in water, H$_2$O molecules accumulate to the hydrophilic edges and defects of MoS$_2$ flakes and replace the Si-S dipole-dipole bonds with Si-H$_2$O and S-H$_2$O hydrogen bonds and attaches to the clean S and Si atoms at the interface. The intercalation and accumulation of H$_2$O molecules at the interface detaches MoS$_2$ flakes from SiO$_2$/Si substrate. Various solvents including hexane, chloroform, acetone, N, N-dimethylformamide, isopropyl alcohol, ethanol and de-ionized water have been tested for their detaching ability. After soaking MoS$_2$/SiO$_2$/Si pieces respectively, only polar protic solvents (isopropyl alcohol, ethanol and de-ionized water) lift the edges of MoS$_2$ flakes off SiO$_2$ noticeably (Figure S1). Isopropyl alcohol and ethanol have slower and subtler lift-off compared to water. Water causes a large amount of MoS$_2$ lifting from both the edges and some vacancies within the flakes. MoS$_2$ is unaffected by non-polar and slightly polar solvents (hexane and chloroform) and polar aprotic solvents (acetone and DMF). Polar protic solvents (ethanol and water) dropped on MoS$_2$/SiO$_2$/Si surfaces accumulate at the edges of the MoS$_2$ flakes, proving the edges of MoS$_2$ are hydrophilic due to dangling bonds while the SiO$_2$ and MoS$_2$ surfaces are not (Figure S2). Despite clean uncontaminated surface of MoS$_2$ is hydrophilic due to lone pair of electrons at the surface,[30] MoS$_2$/SiO$_2$/Si exposed in air for many days is hydrophobic. The contact angle measured on the aged MoS$_2$/SiO$_2$/Si shows a water contact angle of 89.6^o (Figure S2 (b)). This wettability transition with aging was explained by water and hydrocarbon contamination by Chow et al.[31]

Ascorbic acid as a weak reducing agent reduces exposed Mo(IV) atoms at the edges, decomposing MoS$_2$ structure, creating unevenness and promoting the formation of nanoribbons. The reaction between a reducing agent and MoS$_2$ has been observed previously with AgNO$_3$.[32] The interaction between MoS$_2$ and ascorbic acid was confirmed via Raman spectroscopy and x-ray photoemission spectroscopy (XPS).

Raman mapping (E$_{2g}$ peak at 380 cm^{-1}) was used to compare MoS$_2$ as grown, soaked in 0.5 M ascorbic acid DMF solution,

and in 1.5 mM ascorbic acid in H$_2$O to observe the functions of different components of the etching solution (Figure 1 (b)). Before soaking, pristine MoS$_2$ has very little defects, as confirmed by both Raman mapping and optical microscopy images. However, after soaking in ascorbic acid in DMF for 20 minutes, defects start to develop at the edges of each MoS$_2$ flake, indicating the reduction of exposed Mo (IV) at the edges by the ascorbic acid and disintegration of the structure. The preferred binding and reaction at the edges has also been observed in other literature, with oxygen and for water-splitting reactions.[33] The reducing agents expand the defect sites on the MoS$_2$ flake and increase the density of MoS$_2$ nanoribbons (shown schematically in Figure 1 (c)).

XPS was performed on the product of exfoliated MoS$_2$ powder soaked in ascorbic acid water solution for 12 hours. Exfoliated MoS$_2$ powder was used instead of CVD grown monolayers to ensure high enough signal intensity. The results show that 71% of the Mo(IV) has been turned into Mo(VI) as shown in Figure 1 (d). This is caused by reduction of Mo to a lower oxidation state and later oxidizing it to MoO$_3$ hydrate in water under atmosphere. Sulfur from the product shows peaks from sulfate (64%), sulfinyl (15%) together with MoS$_2$ (21%), indicating that the sulfur in MoS$_2$ got oxidized into sulfate and sulfinyl. C 1s spectra of as-bought ascorbic acid was compared with the C 1s spectra of MoS$_2$/ascorbic acid reaction product (Figure S4). C=O: C-O-C, C-O-H ratio increased from 0.25 to 0.76 after the reaction. Despite the carbon spectra cannot be quantified due to contamination, it can qualitatively prove conversion of C-OH bond to C=O during ascorbic acid oxidation.

Reducing agents with different reducing strengths have been tested out, as shown in Figure S5. DIW without any reducing agent gives the least amount of lifting. The nanoribbons formed are stubby and mostly at the edges. However, with increasing reducing strengths, the lifting become much more significant and nanoribbons start to appear within the MoS$_2$ flakes. The strongest reducing agent, NaBH$_4$, produces the thinnest MoS$_2$ nanoribbons. Formaldehyde leaves low density of very thin ribbons and weaker reducing agents like sodium thiosulfate and ascorbic acid gives thicker, higher density ribbons.

The competing kinetics of ascorbic acid etching and MoS$_2$/SiO$_2$ detaching allows MoS$_2$ monolayers to tear instead of being lifted off the surface entirely. A theoretical calculation done by Li *et al.* shows the weakest ultimate

strength and strain within both MoS_2 and $MoSe_2$ are along the zigzag direction at (16.9 GPa, 0.19 and 12.86 GPa, 0.16).[34] A study on MoS_2 monolayers transferred onto Si/SiO_2 surface measured adhesion energy between the two materials to be 0.17 J/m^2,[35] which is much lower than the weakest strength within MoS_2 flakes. However, since the MoS_2 flakes used in this experiment were directly grown with CVD under Ar/H_2 atmosphere, the contaminant between the MoS_2 flakes and Si wafer was less, thus the bonding is stronger with dipole-dipole bonding between S and Si, in addition to van-der-Waals force. Consequently, with appropriate MoS_2 detaching speed and etching kinetic, MoS_2 can be torn into ribbon like form in an aqueous solution of reducing agents. The quality of CVD grown MoS_2 flakes also have an influence on the dimensions of MoS_2 nanoribbons. MoS_2 flakes grown with more defects tend to etch faster, leaving lower density, thinner nanoribbons. If the flakes have large grain size, long ribbons will form.

Figure 2 (a) shows optical microscopy images of the nanoribbons before and after conversion. The ribbons are anisotropic and have width down to the sub-micron regime. The ribbons mostly start from the edge of the 2D MoS_2 flakes and can extend across the entire diameter of the 2D parent. The dimensions of the nanoribbons were measured with an atomic force microscope (AFM) and are shown in Figure 2 (b). The depth profile of a single ribbon is shown in figure 2 (b)(i), where the nanoribbon has a width of 300 ± 50 nm, and a height of 1.5 nm, indicating it is composed of monolayer MoS_2.[36] An AFM map of several nanoribbons is shown in Figure 2 (b)(ii), demonstrating that the ribbons are monolayer or bilayer across their entire length and grow parallel to one another. Scanning electron microscope (SEM) images in Figure 2 (c) shows the width of the nanoribbons is not uniform and can change in ~30° steps. The tearing of MoS_2 is independent of the flow direction of water and only parallel to one of the edges of 2D parent MoS_2 (Figure S8).

Figure 2. (a) Before and after optical microscopy images of MoS_2 treated with 1.5 mM ascorbic acid solution (scale bar: 100 μm). Before treatment (i) triangles and polygonals with no obvious defects are observed. After treatment (ii) ribbons form where the 2D materials used to be. (b) AFM of MoS_2 nanoribbons prepared. (i) Depth profile of a single MoS_2 ribbon along the line indicated in (ii). The width of the nanoribbon measured is 300 nm. (ii) AFM height map of several MoS_2 nanoribbons (scale bar: 1 μm). The group of ribbons generated are parallel to each other. (c) SEM image of MoS_2 nanoribbons (scale bar: 20 μm). The nanoribbons' width vary from 1 μm to 50 nm. (d) Raman and PL mapping of the nanoribbons on Si/SiO_2 substrate. (i) Raman intensity mapping at 380 cm^{-1}. The ribbons show strong and clear intensity as compared to the background, indicating high quality of the MoS_2 lattice. (ii) Raman intensity mapping at 402 cm^{-1}. (iii) PL mapping at 1.82 eV. (e) Box and whisker graph of the aspect ratio of the nanoribbons produced by 0.5 mM, 1.0 mM, and 2.5 mM ascorbic acid. Nanoribbons produced by 0.5 mM ascorbic acid have the
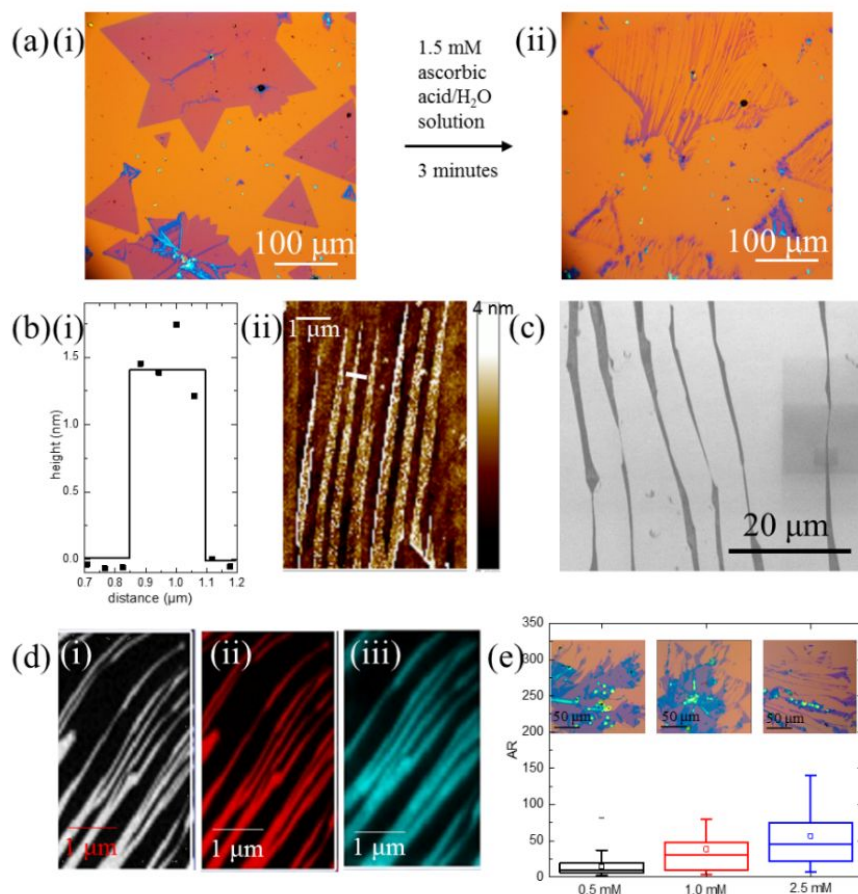
first and third quartile at 5.6 and 19. Mean and median AR are 14 and 10. Nanoribbons produced by 1.0 mM ascorbic acid have the first and third quartile at 11 and 47. Mean and median AR are 38 and 30. Nanoribbons produced by 2.5 mM ascorbic acid have the first and third quartile at 24 and 85. Mean and median AR are 57 and 45. Insets: optical images of MoS_2 flakes after etching with respective concentration of ascorbic acid (scale bar: 50 µm).

The structural integrity of the ribbons was investigated with Raman spectroscopy and photoluminescence (PL). The Raman spectra has peaks at 380 cm^{-1} and 402 cm^{-1}, and Figure 2 (d) shows maps of the Raman intensity at those wavenumbers (380 cm^{-1}-i and 402 cm^{-1}-ii). The Raman maps show uniform intensity over the entire ribbon, indicating MoS_2 ribbons are clean and defect free. Figure 1 (d)(iii) shows the PL map of the peak emission at 1.82 eV. The PL mapping also shows uniform intensity, confirming that the MoS_2 structure is not disturbed.

The dimensions of the nanoribbons can be controlled with the concentration of ascorbic acid, using similar quality CVD grown MoS_2 sheets. Higher concentration of ascorbic acid etches away larger portions of MoS_2 flakes (Figure S9), producing thinner and longer nanoribbons. Figure S9 (f) shows the width and length distribution of nanoribbons when treated with different concentrations of ascorbic acid (0.5 mM, 1.0 mM, and 2.5 mM) for 3 minutes. When the concentration of the ascorbic acid increases, the width decreases. The median of the nanoribbon width decreases from 1316 nm to 950 nm, and 684 nm. An increase of ascorbic acid concentration increases nanoribbons length. The aspect ratio box graph from figure 2 (e) shows that lower concentration of ascorbic acid produces stubbier nanoribbons while higher concentration of ascorbic acid etches MoS_2 flakes into lankier nanoribbons.

Transmission electron microscopy (TEM) images of the MoS_2 before and after turning into nanoribbons are presented in **Figure 3 (a-b)**. Figure 3(b) shows a single post-treatment ribbon, less than 100 nm wide. The edges of the nanoribbon are parallel over the ribbon.
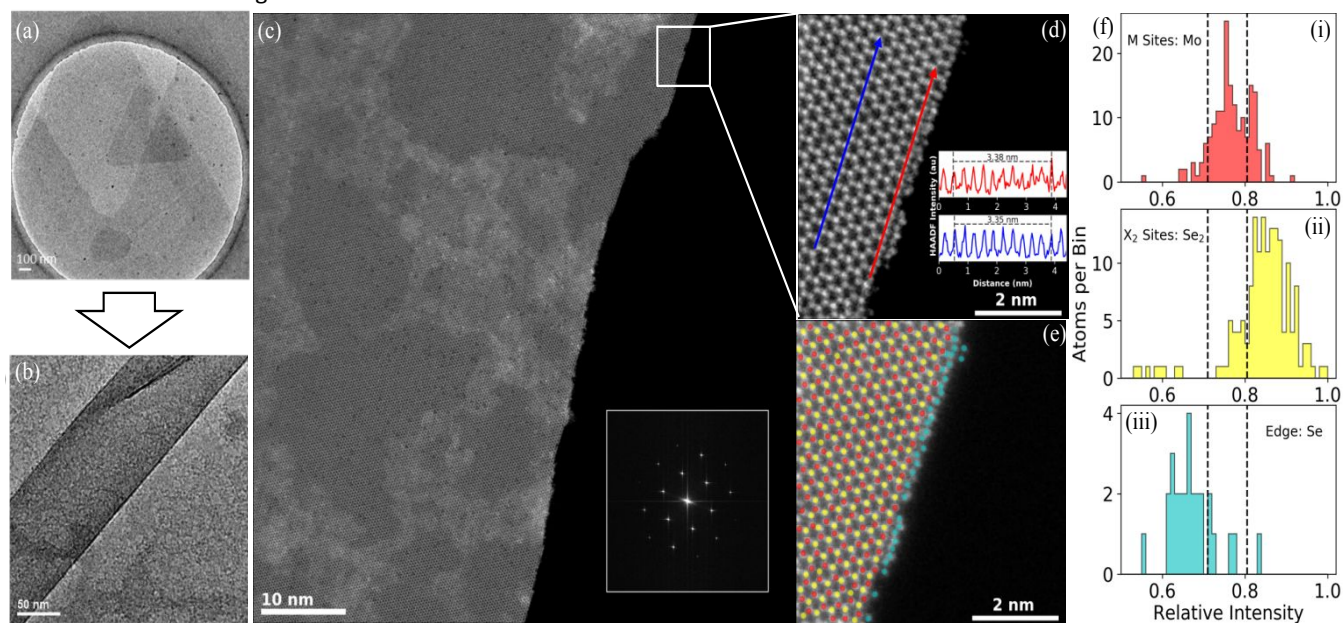

Figure 3. TEM and STEM of MoS_2 and $MoSe_2$ nanoribbons. (a) Transmission electron microscope (TEM) image of a MoS_2 flake before treatment. (b) MoS_2 nanoribbon from sample after treatment. (c) High-angle annular dark-field (HAADF) scanning transmission electron microscopy (STEM) image of $MoSe_2$ nanoribbons. Inset shows fast Fourier transform (FFT) of HAADF-STEM image, demonstrating the entire ribbon is single crystal. (d) High resolution, Z-contrast HAADF-STEM image of $MoSe_2$ nanoribbon edge. The edge is along zigzag direction with defects and disorders among the outmost atoms. Line profiles along the zigzag direction both at the edge (red) and within the bulk (blue) show that the distance between Se_2 columns changes from 3.35 Å (bulk) to 3.38 Å (edge). (e) STEM image from (d) sorted into metal sites (red), chalcogenide sites (yellow), and edge sites (blue) and labeled by color. (f) HAADF intensity histogram of the sorted atoms from (e). Metal and chalcogenide sites show intensities matching well with their Z-values (Mo: Z=42 and Se_2: Z_{eff}=51), while intensity of edge sites too low to be either Mo or Se_2 indicating there are single Se atoms (Z=36) and that the edges are Se terminated.

Nanoscale Horizons

COMMUNICATION

In Figure 3 (c) a high angle annular dark field (HAADF) scanning transmission electron microscopy (STEM) image shows an atomic-resolution picture of a $MoSe_2$ nanoribbon. In the inset is the fast Fourier transform (FFT) of the ribbon. The Fourier points of a single hexagonal structure are clearly observed indicating that the lattice is single crystal with few defects. Figure 3 (d) shows a higher-resolution picture of the edge of the nanoribbon in Figure 3 (c), illustrating that the growth direction mostly coincides with the zigzag-direction. The angle between the edge of the ribbons and the edge of MoS_2 parental flake has been measured via optical microscopy as well (Figure S11). Among 120 measurements, the direction of MoS_2 nanoribbons growth was highly selective and occurred at 62.5º - 67.5º to the edge of the flake, which corresponds to the angle of a zigzag edge, corroborating the STEM analysis. This type of anisotropic degradation has also been observed in WS_2 under laser irradiation.[37]

Line profiles of the HAADF image measure a lattice strain of ~1% at the edge. The two line profiles shown in the inset of Figure 3 (d) are along the growth direction on the Se_2 columns. The average distance over 10 atomic sites is 3.35 Å (bulk) to 3.38 Å (edge).

The edge-termination is determined by measuring the HAADF intensity of the different atomic sites. HAADF imaging uses Z-contrast, meaning heavier atomic columns are brighter than the lighter atomic columns. In order to identify the species at the edge, the atomic columns in Figure 3 (d) are sorted into three categories: metal sites (red), chalcogenide sites (yellow), and edge sites (blue). Then a histogram of the HAADF intensities of each type of site is shown in Figure 3 (f). The metal sites and chalcogenide sites are shown in Figure 3 (f-i) and (f-ii) respectively, and match well with the predicted intensities from Z-values of each element (Mo: Z=42, Se_2: Z_{eff}=51). The intensity of the edge sites is shown in Figure 3 (f-iii) and are distributed of lower intensities than either Mo or Se_2 indicating they are single Se atoms (Z=36), indicating that the $MoSe_2$ nanoribbons are chalcogenide terminated.

The effect of the reduced dimensionality of MoS_2 nanoribbons was further studied through Raman spectroscopy and PL (**Figure 4**). To measure the Raman spectra of the nanoribbons accurately, a laser has been swept across the ribbons as shown in Figure 4 (a). The Raman spectrum across a single 160 nm wide nanoribbon is shown in Figure 4 (b), where a change of position and intensity of Raman peaks (from the center to the edge: dark to light) is observed. Due to much larger size of laser spot size with respect to the nanoribbon width, moving the laser further away from the ribbon reduces the intensity, while allowing the signal from the nanoribbon edge to have a more significant effect. The E_{2g} peak shifts to a lower wavenumber as the laser

spot moves further away, while the A_{1g} peak is unchanged. A shift of ~1 eV for the E_{2g} peak indicates the nanoribbon have around 1% strain at the edge according to the calculation by Rice et al., which agrees with the result obtained from STEM.[38]
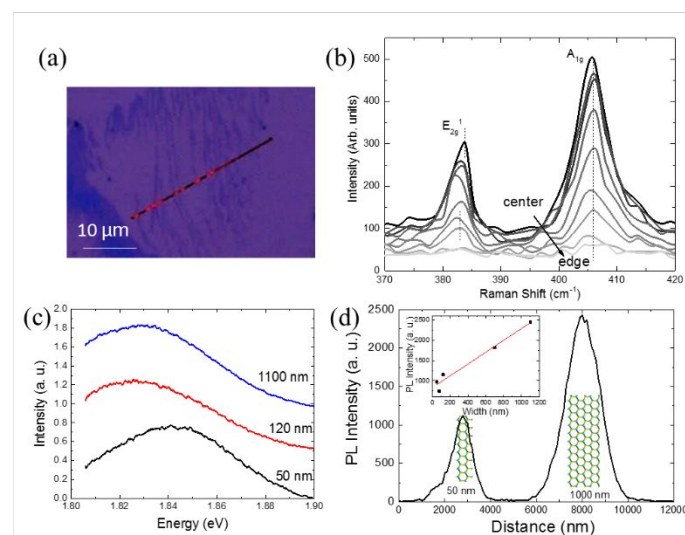

Figure 4. Raman spectroscopy and PL characterization of MoS_2 nanoribbons. (a) Schematic of laser path for Raman and PL measurements. To obtain location dependent spectra, a laser is scanned across multiple nanoribbons. (b) Raman spectrum of a 160 nm MoS_2 nanoribbon from center (dark) to edge (light). Step size: 100 nm. Raman signal intensity decreases as laser spot moves away from the center. (c) PL profiles of nanoribbons with different width. Most nanoribbons have a band gap of 1.82 eV but thinner ribbons were observed to occasionally blue shift to between 1.82 eV and 1.85 eV, possibly due to higher concentrations of defects. (d) PL intensity at 1.82 eV for two ribbons with width of 50 nm and 1000 nm. Intensity drops sharply at the edges of the ribbons. Inset: PL intensity versus ribbon thickness. The intensity increases linearly with width.

Most nanoribbons show a bandgap of 1.82 eV while for ribbons below 100 nm a blue-shift to 1.84 eV is observed, likely due to higher density of defects in the ribbon (Figure 4 (c)). Figure 4 (d) shows PL intensity profile at 1.82 eV across two nanoribbons, 50 and 1000 nm wide. The thicker ribbon predictably shows a higher intensity, and by measuring the intensities of a series of ribbons, a linear relationship between the PL and nanoribbon width can be found. The inset in Figure 4 (d) shows a series of such measurements and demonstrates that PL intensity increases with the thickness of nanoribbons

with a rough linear relationship. This linear relationship can help identify nanoribbon width from PL.

The same method can be applied to CVD grown $MoSe_2$ (Figure S12). The $MoSe_2$ ribbons are partially monolayer (1 nm) and partially bilayer (1.7 nm) (Figure S6).[8]

Experimental Section

MoS_2 and $MoSe_2$ thin films were grown on SiO_2/Si substrates by CVD method. MoO_3 powder was placed in the bottom of a ceramic boat, above which a SiO_2/Si substrate lied face down. The entire boat was then inserted into the center of a quartz tube in a furnace. Another ceramic boat containing S or Se powder was placed upstream of the SiO_2/Si substrate. The furnace was heated up to 750 °C in 15 mins and remained at 750 °C for another 15 mins before cooled down naturally. Ar/H_2 (15% H_2) was used as the carrier gas during the growth process. The CVD grown MoS_2 monolayers were stored in air-tight glass vials before treatment.

To etch monolayer MoS_2, 300 μL of freshly prepared 0.05 M, L-ascorbic acid (Sigma Aldrich, reagent grade) aqueous solution was dropped in 10 mL de-ionized water. MoS_2 wafer was then immersed in the solution for 3 minutes. Then, the wafer was picked out of the solution and submerged in 20 mL de-ionized water for 5 seconds and air dried. To change the concentration of ascorbic acid in the end solution, different volume of 0.05 M ascorbic acid was added (100 μL, 200 μL, and 500 μL). The same MoS_2 wafer was cut into multiple pieces for batch comparison to keep the results accountable. For other reducing agents (iron(II) sulfate, sodium thiosulfate, formaldehyde, sodium borohydride, all from Sigma Aldrich), the same procedure was executed as with ascorbic acid. To study the effect of solvents, the above condition was kept the same (300 μL of freshly prepared 0.05 M L-ascorbic acid in 10 mL of solvents, soak for 3 minutes) except the water was replaced with hexane, chloroform, acetone, N, N-dimethylformamide, isopropyl alcohol, or ethanol (all from Sigma Aldrich).

The synthesized MoS_2 were first observed under optical microscope. AFM (Bruker Multimode 8) was conducted under ScanAsyst™ self-optimizing mode. FEI Quanta 400 ESEM was used to take higher magnification images of the nanoribbons on Si wafer under 10 V beam voltage. PHI Quantera XPS was used to study the elemental composition of the end-product between MoS_2 and ascorbic acid. Pass energy used was 26 eV. Raman and PL spectrum were obtained on Renishaw InVia Raman Microscope. Laser wavelength was at 532 nm. To reduce damage to the nanoribbons, laser power was reduced to 10% for Raman and 5% for PL.

For STEM and TEM characterization, the nanoribbons were transferred onto holey carbon coated TEM grids using a PMMA-assisted transferring technique. The sample was spin-coated with PMMA 950K at 2000 rpm for 60 s and then SiO_2

was etched with KOH. PMMA film after being transferred onto TEM grid was washed with acetone and IPA. TEM (JEOL 2010 Transmission Electron Microscope), STEM characterization was performed on a Nion aberration-corrected UltraSTEM 100 operated at 60 kV accelerating voltage.

The angle, width and length of the nanoribbons were measured with ImageJ using 50x optical images. The angles were measured using angle measurement tool. The width was measured by measuring the FWHM of the peak from intensity measurement across and perpendicular to the nanoribbons. The length of the nanoribbons was measured using line measurement tool.

To study the effect of water flow direction to tearing, a MoS_2/SiO_2/Si was placed in a narrow tube and had water flow across in one direction for one minute.

Conclusions

In summary, we have successfully produced a simple but effective way to produce TMDC (MoS_2 and $MoSe_2$) nanoribbons from CVD grown thin layers on Si/SiO_2 wafer. Aqueous solution of reducing agents was used to etch the TMDC flakes. The process works through reducing agents expanding the defects in the TMDC and water detaching TMDC flakes from the SiO_2 surface and tears the layer along its weakest direction, the zigzag direction. The density of the nanoribbons produced can be controlled by adjusting the concentration and the reducing strength of reducing agents. Higher concentration of reducing agent can increase the percentage of TMDC flakes turned into nanoribbons. Stronger reducing agent not only increase the percentage of TMDC film turning into ribbons, but also reduce the width and density of the ribbons synthesized. Raman and HAADF STEM shows an increased strain at the edge of each ribbon. An increase of bandgap has been observed for MoS_2 nanoribbons down to 50 nm and PL intensity can be used to estimate nanoribbon width. This method provides a solution towards producing a large area of nanoribbons economically and efficiently.

Conflicts of interest

There are no conflicts to declare.

Acknowledgements

Notes and references

1. S. Z. Butler, S. M. Hollen, L. Cao, Y. Cui, J. A. Gupta, H. R. Gutiérrez, T. F. Heinz, S. S. Hong, J. Huang, A. F. Ismach, E. Johnston-Halperin, M. Kuno, V. V. Plashnitsa, R. D. Robinson, R. S. Ruoff, S. Salahuddin, J. Shan, L. Shi, M. G. Spencer, M. Terrones, W. Windl and J. E. Goldberger, *ACS Nano*, 2013, **7**, 2898-2926.
2. M. Chhowalla, D. Jena and H. Zhang, 2016, **1**, 16052.
3. J. Huang, Z. Wei, J. Liao, W. Ni, C. Wang and J. Ma, Journal of Energy Chemistry, 2018, doi:10.1016/j.jechem.2018.09.001.
4. Q. H. Wang, K. Kalantar-Zadeh, A. Kis, J. N. Coleman and M. S. Strano, *Nat Nano*, 2012, **7**, 699-712.
5. G. He, K. Ghosh, U. Singisetti, H. Ramamoorthy, R. Somphonsane, G. Bohra, M. Matsunaga, A. Higuchi, N. Aoki, S. Najmaei, Y. Gong, X. Zhang, R. Vajtai, P. M. Ajayan and J. P. Bird, *Nano Letters*, 2015, **15**, 5052-5058.
6. S. Najmaei, S. Lei, R. A. Burke, B. M. Nichols, A. George, P. M. Ajayan, A. D. Franklin, J. Lou and M. Dubey, 2016, **6**, 39465.
7. F. Liu, S. Zheng, X. He, A. Chaturvedi, J. He, W. L. Chow, T. R. Mion, X. Wang, J. Zhou, Q. Fu, H. J. Fan, B. K. Tay, L. Song, R.-H. He, C. Kloc, P. M. Ajayan and Z. Liu, *Advanced Functional Materials*, 2016, **26**, 1169-1177.
8. K. Keyshar, Y. Gong, G. Ye, G. Brunetto, W. Zhou, D. P. Cole, K. Hackenberg, Y. He, L. Machado, M. Kabbani, A. H. C. Hart, B. Li, D. S. Galvao, A. George, R. Vajtai, C. S. Tiwary and P. M. Ajayan, *Advanced Materials*, 2015, **27**, 4640-4648.
9. X. Wang, Y. Gong, G. Shi, W. L. Chow, K. Keyshar, G. Ye, R. Vajtai, J. Lou, Z. Liu, E. Ringe, B. K. Tay and P. M. Ajayan, *Acs Nano*, 2014, **8**, 5125-5131.
10. Z. Wang, V. Kochat, P. Pandey, S. Kashyap, S. Chattopadhyay, A. Samanta, S. Sarkar, P. Manimunda, X. Zhang, S. Asif, A. K. Singh, K. Chattopadhyay, C. S. Tiwary and P. M. Ajayan, *Advanced Materials*, 2017, **29**, 1700364.
11. J. Shen, Y. He, J. Wu, C. Gao, K. Keyshar, X. Zhang, Y. Yang, M. Ye, R. Vajtai, J. Lou and P. M. Ajayan, *Nano Letters*, 2015, **15**, 5449-5454.
12. Y. Kim, J.-G. Song, Y. J. Park, G. H. Ryu, S. J. Lee, J. S. Kim, P. J. Jeon, C. W. Lee, W. J. Woo, T. Choi, H. Jung, H.-B.-R. Lee, J.-M. Myoung, S. Im, Z. Lee, J.-H. Ahn, J. Park and H. Kim, *Scientific Reports,* 2016, **6**, 18754.
13. Z. Liu, L. Ma, G. Shi, W. Zhou, Y. Gong, S. Lei, X. Yang, J. Zhang, J. Yu, K. P. Hackenberg, A. Babakhani, J.-C. Idrobo, R. Vajtai, J. Lou and P. M. Ajayan, *Nature Nanotechnology*, 2013, **8**, 119-124.
14. J. Liang, Z. Wei, C. Wang, J. Ma, *Electrochimica Acta*, 2018, **285,** 301-308.
15. Z. Liu and K. Aydin, *Nano Letters*, 2016, **16**, 3457-3462.
16. J. Kim, W. S. Yun and J. D. Lee, *The Journal of Physical Chemistry C*, 2015, **119**, 13901-13906.
17. C.-H. Lee, J. Lin and C.-K. Yang, *Scientific Reports*, 2018, **8**, 13307.
18. Y.-N. Wen, M.-G. Xia and S.-L. Zhang, *Physics Letters A*, 2018, **382**, 2354-2360.
19. L. Wang, H. Dong, Z. Guo, L. Zhang, T. Hou and Y. Li, *The Journal of Physical Chemistry C*, 2016, **120**, 17427-17434.
20. Z. Zhang, Y. Xie, Q. Peng and Y. Chen, *Scientific Reports*, 2016, **6**.
21. A. N. Abbas, G. Liu, B. Liu, L. Zhang, H. Liu, D. Ohlberg, W. Wu and C. Zhou, *Acs Nano*, 2014, **8**, 1538-1546.
22. S. Yang, D. Li, T. Zhang, Z. Tao and J. Chen, *The Journal of Physical Chemistry C*, 2012, **116**, 1307-1312.
23. Y. Pak, N. Lim, Y. Kumaresan, R. Lee, K. Kim, T. H. Kim, S.-M. Kim, J. T. Kim, H. Lee, M.-H. Ham and G.-Y. Jung, *Advanced Materials*, 2015, **27**, 6945-6952.
24. Y. Li, Z. Zhou, S. Zhang and Z. Chen, *Journal of the American Chemical Society*, 2008, **130**, 16739-16744.
25. L.-U. Florentino, E. Ana Laura, P.-L. Néstor, R. G. Humberto, T. Mauricio and T. Humberto, *2D Materials*, 2015, **2**, 015002.
26. M. H. Heyne, J. F. De Marneffe, A. Delabie, M. Caymax, E. C. Neyts, I. Radu, C. Huyghebaert and S. De Gendt, *Nanotechnology*, 2017, **28**.
27. Z. Wang, H. Li, Z. Liu, Z. Shi, J. Lu, K. Suenaga, S. K. Joung, T. Okazaki, Z. Gu, J. Zhou, Z. Gao, G. Li, S. Sanvito, E. Wang and S. Iijima, *Journal of the American Chemical Society*, 2010, **132**, 13840-13847.
28. Y. Pak, Y. Kim, N. Lim, J.-W. Min, W. Park, W. Kim, Y. Jeong, H. Kim, K. Kim, S. Mitra, B. Xin, T.-W. Kim, I. S. Roqan, B. Cho and G.-Y. Jung, *APL Materials*, 2018, **6**, 076102.
29. L. Vieira, J. d. R. Martins Neto, O. P. Ferreira, R. M. Torresi, S. I. Cordoba de Torresi and O. L. Alves, *RSC Advances*, 2018, **8**, 30346-30353.
30. S. Lei, X. Wang, B. Li, J. Kang, Y. He, A. George, L. Ge, Y. Gong, P. Dong, Z. Jin, G. Brunetto, W. Chen, Z.-T. Lin, R. Baines, D. S. Galvão, J. Lou, E. Barrera, K. Banerjee, R. Vajtai and P. Ajayan, *Nature Nanotechnology*, 2016, **11**, 465.
31. P. K. Chow, E. Singh, B. C. Viana, J, Gao, J. Luo, J. Li, Z. Lin, A. L. Elias, Y. Shi, Z. Wang, M. Terrones and N. Koratkar, *ACS Nano,* 2015, *9* **(3),** 3023-3031.
32. B. Mondal, A. Som, I. Chakraborty, A. Baksi, D. Sarkar and T. Pradeep, *Nanoscale*, 2016, **8**, 10282-10290.
33. H. Nan, Z. Wang, W. Wang, Z. Liang, Y. Lu, Q. Chen, D. He, P. Tan, F. Miao, X. Wang, J. Wang and Z. Ni, *Acs Nano*, 2014, **8**, 5738-5745.
34. J. Li, N. V. Medhekar and V. B. Shenoy, *The Journal of Physical Chemistry C*, 2013, **117**, 15842-15848.
35. S. Deng, E. Gao, Z. Xu and V. Berry, *ACS Applied Materials & Interfaces*, 2017, **9**, 7812-7818.
36. I. Bilgin, F. Liu, A. Vargas, A. Winchester, M. K. L. Man, M. Upmanyu, K. M. Dani, G. Gupta, S. Talapatra, A. D. Mohite and S. Kar, *Acs Nano*, 2015, **9**, 8822-8832.
37. Z. Mutlu, M. Ozkan and C. S. Ozkan, *Materials Chemistry and Physics*, 2016, **176**, 52-57.
38. C. Rice, R. J. Young, R. Zan, U. Bangert, D. Wolverson, T. Georgiou, R. Jalil and K. S. Novoselov, *Physical Review B*, 2013, **87**, 081307.